Engineering and Computational Mechanics
Volume 166 Issue EM4

Computational fluid dynamics of vortex flow controls at low flow rates
Queguineur, Jarman, Paterson and Tabor

ice | proceedings

Proceedings of the Institution of Civil Engineers
Engineering and Computational Mechanics 166 December 2013 Issue EM4
Pages 211–221 http://dx.doi.org/10.1680/eacm.12.00017
Paper 1200017
Received 27/09/2012 Accepted 06/06/2013
Keywords: fluid mechanics/hydraulics & hydrodynamics/sewers & drains

ice Institution of Civil Engineers publishing

Computational fluid dynamics of vortex flow controls at low flow rates

Gautier Queguineur MEng
Undergraduate student, College of Engineering, Maths and Physical Sciences, University of Exeter, Exeter, UK

Daniel Jarman MEng
Product Development Specialist, Hydro International plc, Clevedon, UK

Eric Paterson MS, PhD
Professor and Department Head, Aerospace and Ocean Engineering, Virginia Polytechnic Institute and State University, Blacksburg, VA, USA

Gavin Tabor MSc, PhD
Senior Lecturer in Computational Fluid Dynamics, College of Engineering, Maths and Physical Sciences, University of Exeter, Exeter, UK

A vortex flow control with differing outlet shapes is investigated computationally at low flow rates. The volume of fluid method was utilised to track the moving free surface. In order to achieve a smooth free surface, interface compression coupled with the inter-gamma compressive scheme was used. The turbulent evolution of the two-phase flow was modelled by solving the Reynolds-averaged Navier–Stokes equations with the k–ε model for turbulent quantities. Validation of the results was carried out by analysing the total head and discharge coefficient for the three outlet shapes at various flow rates and comparing these results with experimental data. Very good agreement with the experimental data was obtained.

Notation

A	outlet area
C_o	Courant number
C_d	discharge coefficient
C_μ, $\sigma_{k,\varepsilon}$, $C_{1\varepsilon,2\varepsilon}$	k–ε model coefficients
D_0	VFC outlet diameter
D_i	diodicity
Eu	Euler number
$\boldsymbol{g}$	gravitational acceleration
H	total head
h	hydraulic head
I	turbulent intensity
k	turbulent kinetic energy
l	characteristic inlet turbulent length scale
p	pressure
Q	volumetric flow rate
$\boldsymbol{R}$	Reynolds stress
Re	Reynolds number
S_{ij}	mean strain
t	time
$\boldsymbol{U}_{rb}$	compressive interface velocity
$\boldsymbol{u}$	flow velocity
α	volume fraction
ε	turbulent dissipation
ν	kinematic viscosity
ρ	density
σ	surface tension
τ	hydrodynamic shear

1. Introduction

Within an urban drainage network it is usually necessary to regulate flow through the system to control the effects of storm surges. This can be done by introducing control elements at critical points in the network, which allow water at normal flow rates through but divert storm surges to attached storage containers for later processing. The ideal control element would have zero resistance to flow for flow rates up to a (specified) cutoff, at which point the flow would be diverted (for instance by a very sharp increase in flow resistance).

Many active and passive controllers have been developed, of which one of the most promising is the vortex flow control (VFC). This is a self-activating device that relies on the properties of the vortex formed at an orifice to regulate the flow. The hydraulic behaviour of these devices is influenced by their geometry and orientation. When the VFC is positioned so that the discharge direction is horizontal, it exhibits a bi-stable characteristic. For low velocities the gravitational effects are dominant and normal orifice-type flow patterns develop. As the flow rate and azimuthal velocity increase, a vortex forms that results in additional inertial and turbulent losses across the VFC due to the swirling motion and thus a substantial increase in head loss in the system. The transition between these two bi-stable modes – referred to as the 'kick-back phase' – is not smooth, which results in a complex hydraulic characteristic for the VFC. The bi-stable behaviour of VFCs offers the benefits associated with a feedback-controlled, automated penstock without the associated power and maintenance requirements. Parsian and Butler (1993) analysed the hydraulic behaviour of conical-type VFCs and suggested that, compared with an orifice, storage volume savings of 25% are attainable.

Many proprietary VFC designs exist and they have grown to be relatively common devices in urban drainage systems, with over

15 000 confirmed installations in the UK (LeCornu and Faram, 2006). It is hypothesised that the bi-stable hydraulic characteristic can be tailored to deliver behaviour approaching the constant discharge relationship by modifying the VFC geometry. Kulkarni *et al.* (2008) published a concise compilation of clear guidelines for the design and optimisation of VFC units based on experimental studies of flow and pressure drop covering a wide range of designs. The effects of outlet configuration on the performance of VFCs were investigated using computational and experimental methods, and expressed in terms of the diodicity $D_i = Eu_r/Eu_f$, where Eu_r and Eu_f are the reverse and forward flow Euler numbers. The variation of diodicity with respect to the Reynolds number was shown to level out above a critical Reynolds number Re_{cr}, the value of which was seen to increase with the unit size.

The intention of this paper is to present a computational investigation of the flow through a VFC at low flow rates, where vortexing is not occurring and water simply flows in through the inlet and out through the outlet orifice as shown in Figure 1(a). In this regime there is a free surface flow and the flow through the outlet orifice is largely similar to flow over a thin plate weir. The behaviour of a VFC in the vortex flow regime has been investigated previously, albeit not extensively (Deamer, 1988; Green, 1988; Parsian and Butler, 1993; Priestman, 1987; Wojtowicz and Kotowski, 2009). Much less work has been done to investigate the flow at low flow rates – in fact, it is the authors' belief that the current work is the first attempt to analyse thoroughly this regime computationally. The aim of the paper is to present the results of computational fluid dynamics (CFD) simulation using the volume of fluid (VOF) method to investigate the free surface flow through a typical VFC. To extend the work, the effect of varying the shape of the outlet was investigated, with a standard circular outlet compared with an inverted triangle and a square of the same outlet area. The CFD results were compared with in-house experimental data (Worrall, 2011) taken using a specially constructed testing rig sited at Hydro International's experimental facility at Clevedon, UK (Jarman, 2011; LeCornu and Faram, 2006).

1.1 Literature survey

Although very little has been done in the past to analyse VFCs in the orifice flow regime, equivalent flows have been investigated. In particular, the flow through an orifice in this regime is effectively flow over a thin plate weir, and this is an area of great interest to civil engineers. This section considers some previous attempts to model flow over weirs using computational methods, as an illustration of the likely quality of results that can be obtained.

Sarker and Rhodes (2004) compared measurements of the free surface profile over a laboratory-scale, rectangular broad-crested weir with numerical calculations using the commercial software Fluent V.4.4.7. The experimental set-up consisted of a flow discharging over a brick and downward ramp into a sump. The height of the free surface above bed level was measured using a pointer-gauge/Vernier scale and Fluent was used to compute the velocity profile over the rectangular broad-crested weir. The VOF method was utilised to compute the air/water interface and the standard k–ε turbulence model was used to solve the turbulent flow for a Reynolds number of 35×10^3. The upstream water level was correctly predicted with a discrepancy of 0·32%. The flow over the weir was also accurately calculated with only a 4·2% error compared with the experimental results. Further downstream, the free surface profile revealed a stationary wave form and slightly underpredicted velocity profiles with a maximum percentage error of 7·1%. This work has therefore shown that the VOF method and the standard k–ε turbulence model can predict complex open-channel flows over a rectangular weir geometry.

Similarly, Qu *et al.* (2009) reported the two-dimensional (2D) numerical simulation of sharp-crested weir flows in a rectangular open channel. The standard two-equation Wilcox k–ω turbulence model was adopted for the numerical simulation of turbulence and, again, the VOF method was utilised to capture the free surface between air and water. The results of the simulations were validated using experimental data of surface profiles, distributions of velocities and pressure heads. Qu *et al.* (2009) concluded that the velocity and pressure head distributions in the nappe region were in very good agreement with the experimental results. The surface profiles of the simulation also agreed with the experimental profiles.

2. Computational methodology

The CFD code adopted for this work was the open-source code OpenFOAM. This solves the governing Reynolds-averaged Navier–Stokes (RANS) equations, the associated turbulence model, plus free surface modelling by means of the VOF methodology using the finite-volume method on arbitrary unstructured polyhedral meshes (Tabor, 2010; Weller *et al.*, 1998). Properly, OpenFOAM is not a CFD code, but a C++ class library for writing CFD codes; the distribution comes with a number of pre-written applications, including several aimed at solving free surface flow problems. In this work, the pre-written solver interFoam was used, which uses the VOF methodology to treat the free surface. Details of the numerical and computational issues are provided below.

2.1 Governing equations

This study adopted the classic RANS methodology of the standard k–ε turbulence model. This is the most widely used turbulence model and has proved very successful in industrial applications. Previous research (e.g. Ferrari, 2010; Qu *et al.*, 2009; Sarker and Rhodes, 2004) has demonstrated the accuracy of the k–ε turbulence model to predict the turbulence of sharp-crested weirs in open channels. Applying an ensemble average to the Navier–Stokes equations for incompressible flow produces the RANS equations

$$1. \quad \nabla . \bar{\boldsymbol{u}} = 0$$

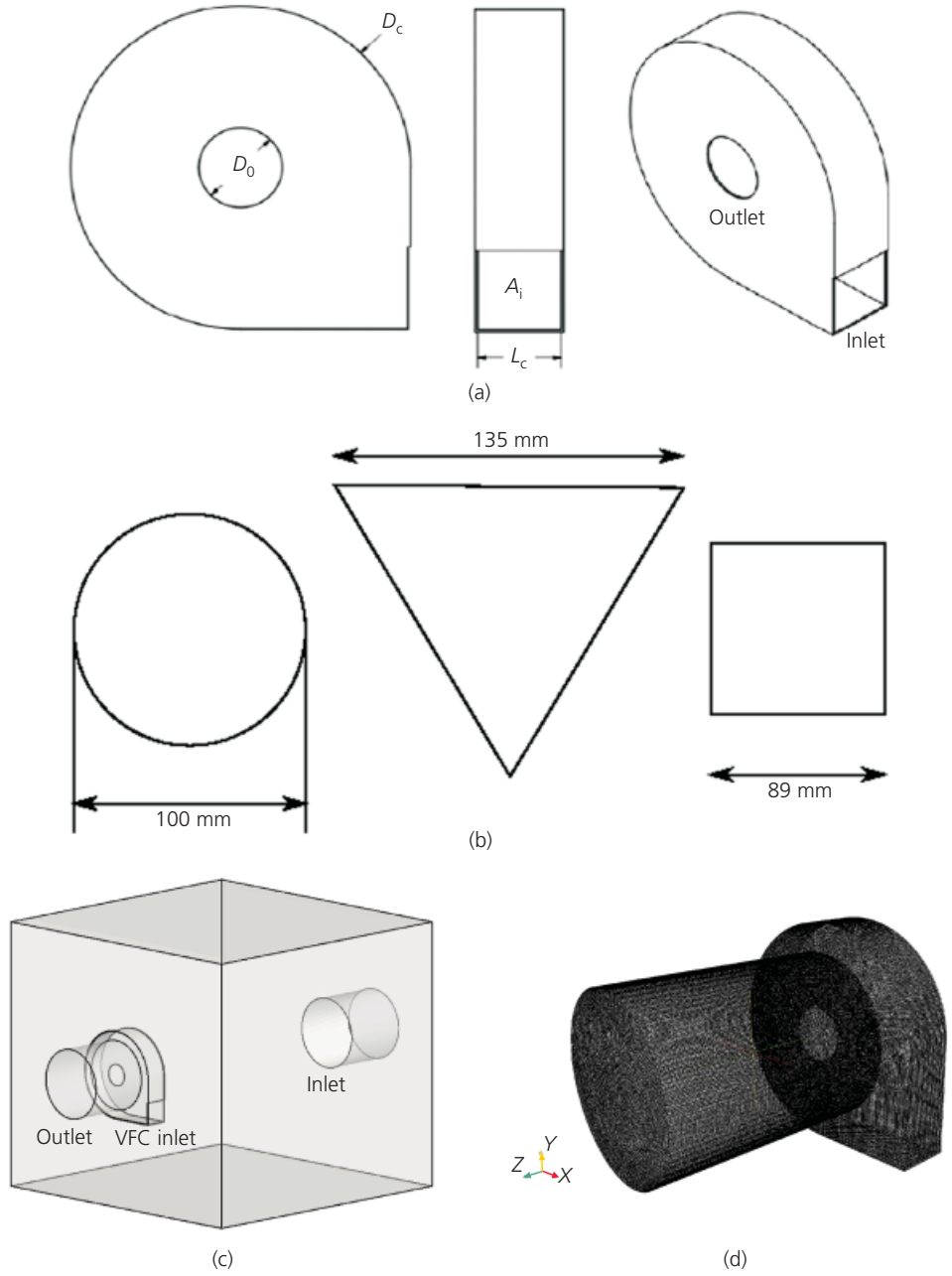

Figure 1. Geometry of the VFC: (a) three views of the basic unit; (b) shapes and orientations of the three outlets (circular, triangular and square); (c) geometry of upper tank in the experimental rig; (d) computational mesh

$$2. \quad \frac{\partial \bar{\boldsymbol{u}}}{\partial t} + \nabla.\bar{\boldsymbol{u}}\bar{\boldsymbol{u}} + \nabla.\boldsymbol{R} = -\frac{1}{\rho}\nabla p + \nabla.\tau$$

where $\tau = \nu(\nabla\bar{\boldsymbol{u}} + \nabla\bar{\boldsymbol{u}}^{\mathrm{T}})$ is the mean viscous stress tensor and $\bar{\boldsymbol{u}}$ is the ensemble average velocity. These are mathematically the same as the laminar Navier–Stokes equations but with an additional term, $\nabla.\boldsymbol{R}$, referred to as the Reynolds stress term, representing the effect of the turbulent component of the flow on the mean flow. This can be modelled using the Boussinesq approximation by introducing the turbulent viscosity ν_t. This is still an unknown quantity and so must be represented by an algebraic or transport equation, or series of equations, relating it to the mean flow variables. The standard k–ε model (Launder and Spalding, 1974) uses transport equations for turbulent

kinetic energy k and turbulent dissipation rate ε that can be defined as

$$\frac{\partial(\rho k)}{\partial t} + \nabla.(\rho k\bar{\boldsymbol{u}}) = \nabla.\left(\frac{\mu_t}{\sigma_k}\nabla k\right) + 2\mu_t S_{ij}.S_{ij} - \rho\varepsilon \quad (3)$$

$$\frac{\partial(\rho\varepsilon)}{\partial t} + \nabla.(\rho\varepsilon\bar{\boldsymbol{u}}) = \nabla.\left(\frac{\mu_t}{\sigma_\varepsilon}\nabla\varepsilon\right) + C_{1\varepsilon}\frac{\varepsilon}{k}2\mu_t S_{ij}.S_{ij} - C_{2\varepsilon}\rho\frac{\varepsilon^2}{k} \quad (4)$$

The model contains five dimensionless coefficients: σ_k, σ_ε, $C_{1\varepsilon}$ and $C_{2\varepsilon}$ from Equations 3 and 4, together with a coefficient C_μ relating the quantities k and ε to the turbulent viscosity ν_t. Values of the coefficients are derived from experimental data over a wide range of turbulent flows and assumed to be constants of the model. Here, the standard values of these coefficients given in Table 1 were used (Launder and Spalding, 1974).

2.2 The VOF method

Hirt and Nichols (1981) introduced the VOF method in order to solve flow problems with moving free surfaces. The evolution of the interface separating two different phases can be described using a discrete function whose value in each cell of the computational domain is equal to the volume fraction α, which is defined as

- $\alpha = 1$, control volume is filled only with phase 1
- $\alpha = 0$, control volume is filled only with phase 2
- $0 < \alpha < 1$, interface present in control volume.

Since the volume fraction α is smoothly varying between 0 and 1, the interface is never sharply defined, but occupies a volume around the region where a sharp interface should exist (Gopala and Wachen, 2007). The evolution of the volume fraction α is governed by the advection equation

$$\frac{\partial\alpha}{\partial t} + \nabla.(\alpha\bar{\boldsymbol{u}}) = 0 \quad (5)$$

It is necessary to solve Equation 5 in such a way as to generate a sharp interface. The discretisation of the advection term must limit numerical diffusion and oscillations at the phase 1/phase 2 interface. Jasak and Weller (1995) introduced a compression term into Equation 5, giving

C_μ	σ_k	σ_ε	$C_{1\varepsilon}$	$C_{2\varepsilon}$
0·09	1·00	1·30	1·44	1·92

Table 1. Coefficient values for k–ε turbulence model

$$\frac{\partial\alpha}{\partial t} + \nabla.(\bar{\boldsymbol{u}}\alpha) + \nabla.(\boldsymbol{U}^r\alpha(1-\alpha)) = 0 \quad (6)$$

where $\boldsymbol{U}^r$ is a velocity field suitable for the compression of the interface. Due to the term $\alpha(1-\alpha)$, the compression term is active only at the interface where the volume fraction α varies between 0 and 1. The solution to the discretised form of Equation 6 is determined using the inter-gamma differencing scheme based on the donor–acceptor method and normalised variable diagram formulated by Leonard (1988). This scheme preserves boundedness of α by introducing a certain amount of numerical diffusion while at the same time preserving a reasonably sharp resolution of the interface.

3. Numerical methods

3.1 Geometry and computational grid

The three main features of the VFC structure are the inlet, outlet and walls. The flow is directed tangentially into the structure through a square inlet (100 mm × 100 mm) and flows out through a sharp-crested weir outlet of 3 mm thickness. The total head was investigated for three different outlet shapes of similar surface area

- circular outlet of 100 mm diameter
- triangular outlet with 135 mm sides
- square outlet with 89 mm sides.

The geometry of the basic VFC unit is shown in Figure 1(a) while Figure 1(b) shows the shapes and orientations of the different exit orifices. The experimental tests were carried out using a test rig sited at the Clevedon Hydro International experimental facility (Jarman, 2011; LeCornu and Faram, 2006), consisting of an upper tank draining into a lower tank. The geometry of the upper tank is shown in Figure 1(c); the VFC is fixed at the outlet to the upper tank and freely discharges into a large-diameter pipe that feeds to the lower tank. Free surface computations provide precise information about multi-phase flow characteristics, but are computationally expensive and require complex grids. Simulating the whole of the upper tank was found to be prohibitively expensive – instead, the computational domain was restricted to the VFC itself (400 mm × 100 mm) and the downstream pipe (300 mm × 400 mm), as shown in Figure 1(d). This had the additional advantage that the inlet to the computational domain was entirely submerged, simplifying the computational inlet boundary condition.

The mesh was generated using the commercial software Gambit. Due to the relative simplicity of the geometry, the Cooper meshing algorithm was used to create an unstructured hexahedral mesh automatically. Hexahedral cells were chosen to minimise the overall number of cells and skewness of the grid. Table 2 summarises the main characteristics of the computational grid.

Overall number of cells	1562994
Hexahedral cells	1562994
Minimum volume: m^3	$5{\cdot}21108 \times 10^{-9}$
Maximum non-orthogonality	18·0868
Average non-orthogonality	2·41466
Maximum skewness	0·437426

Table 2. Mesh characteristics

3.2 Boundary conditions

The inlet velocity was specified according to the volumetric flow rate Q_{in}. Therefore, the inlet velocity can be defined as the ratio of the incoming volumetric flow rate Q_{in} to the area of the inlet patch A_{i}

$$U = \frac{Q_{\text{in}}}{A_{\text{i}}}$$

The investigation of low flow rates comprises incoming volumetric flow rates of water in the range $0{\cdot}5 < Q_{\text{in}} \leqslant 4{\cdot}5$ l/s. The flow becomes turbulent above $Q_{\text{in}} \simeq 0{\cdot}5$ l/s and reaches a maximum Reynolds number $\text{Re} = 45\,000$ for an incoming volumetric flow rate of $Q_{\text{in}} = 4{\cdot}5$ l/s, using a Reynolds number based on the VFC outlet diameter

$$\text{Re} = \frac{4Q}{\nu\pi D_0} \quad (7)$$

In order to satisfy the no-slip boundary conditions, both phases have zero velocity relative to the boundary of the domain. The transmissive behaviour of the outlet patch was achieved by using zero gradient boundary conditions.

In order to accelerate the calculations, the level of water was set above the inlet boundary. The inlet patch was consequently submerged at $t = 0$ with a volume fraction $\alpha_1 = 1$ across the entire patch. The multi-phase formulation solved for $p\_rgh = p - \rho gh$, rather than the static pressure p. This makes the implementation of the boundary conditions easier and also avoids inaccuracies in the handling of the pressure force and buoyant force balance on non-orthogonal and distorted meshes. A fixed value of p_rgh was given at the outlet patch to induce a pressure drop across the domain.

To initialise the flow as turbulent at the inlet, a turbulent intensity $I = 0{\cdot}16 \times \text{Re}^{-1/8}$ was defined. From this, values of turbulent intensity k and turbulent dissipation rate ε were calculated using Equations 8 and 9

$$k = \frac{3}{2}(UI)^2 \quad (8)$$

$$\varepsilon = C_{\mu}^{3/4}\frac{k^{3/2}}{l} \quad (9)$$

where $l = 0{\cdot}07D$ is an appropriate length scale characteristic of the turbulence and $C_{\mu} = 0{\cdot}09$ is a dimensionless constant characteristic of the k–ε transport equations. The National Institute of Standards and Technology standard values of kinematic viscosity and density were used for air and water. The gravitational acceleration is given the standard value $\boldsymbol{g} = (0\ \ -9{\cdot}81\ \ 0)$. The surface tension between the two phases was defined as $\sigma = 0{\cdot}07$ N/m.

3.3 Convergence criteria

Mesh quality and smoothness are essential for both the accuracy and efficiency of numerical simulations. A mesh refinement study was performed to minimise errors due to control volume size. An initial mesh was iteratively refined until the solution of the simulations became grid independent. Optimisation of the grid also saved a considerable amount of computational time, while maintaining constant accuracy. The validation of the mesh was performed by comparing the values of total head H against the overall number of cells. Figure 2 depicts the results of the mesh convergence study for the case $Q = 1{\cdot}5$ l/s. The difference between the total head calculated on 1·56 million cells and 2·04 million cells was 0·089%, so the mesh of 1·56 million cells was used to carry out the simulations.

3.4 Numerical schemes and solution control

The interFoam solver uses the multidimensional universal limiter for explicit solution (Mules) method to ensure boundedness of the volume fraction independent of the underlying numerical scheme. The $\nabla.(\bar{\boldsymbol{u}}\alpha)$ convection term uses the van Leer scheme, which is a strictly bounded scheme with values constrained between 0 and 1. This ensures that the calculated values of the volume fraction are limited to $0 \leqslant \alpha \leqslant 1$. The term $\nabla.(\boldsymbol{U}_{\text{rb}}\alpha)$

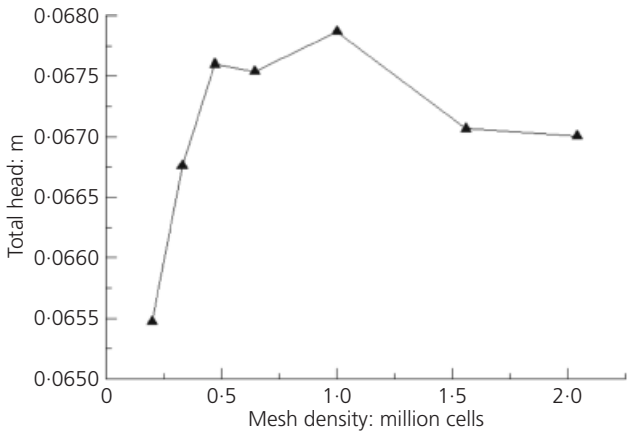

Figure 2. Mesh convergence study comparing total head H against the overall number of cells for $Q = 1{\cdot}5$ l/s

uses the interface compression scheme, where $\boldsymbol{U}_{rb}$ is a compressive velocity normal to the fluid interface. The value of $\boldsymbol{U}_{rb}$ was determined according to Berberovic *et al.* (2009). The rest of the convection schemes were defined first-order accurate upwind to maintain stability. The Euler differencing scheme was used for the first time derivative, while second-order linear differencing was used for the gradient terms. Matrix solution was accomplished using the geometric–algebraic multi-grid (GAMG) solver, while pressure/velocity coupling was through the PISO scheme (Issa, 1985), with four iterations of the interior loop to enhance the stability of the solution.

3.5 Time-step control

Time-step control is essential in free surface tracking modelling since the algorithm is extremely sensitive to the Courant–Friedrichs–Lewy number. The time-step is continuously adjusted to maintain a maximum Courant number of $C_o = 0{\cdot}5$. Figure 3(a) shows a typical graph of time-step δt over time for the circular outlet at $Q = 3$ l/s. The time-step becomes approximately constant when the overall flow velocity approaches steady state. A great amount of computational time can be saved by performing a run-time convergence study. This enables the user to determine an appropriate end time for the simulations. Figure 3(b) depicts the convergence of the total head H against time at six various flow rates for the circular outlet. Since this study focuses on the evolution of total head against flow rate, the simulations can be stopped when the values of total head reach convergence. Similar convergence studies were also carried out for the triangular and square outlets. In order to ensure convergence and accuracy of the results, all the simulations were run for a minimum of 5 s. Higher flow rates were run to 10 s, but no variation in total head was observed.

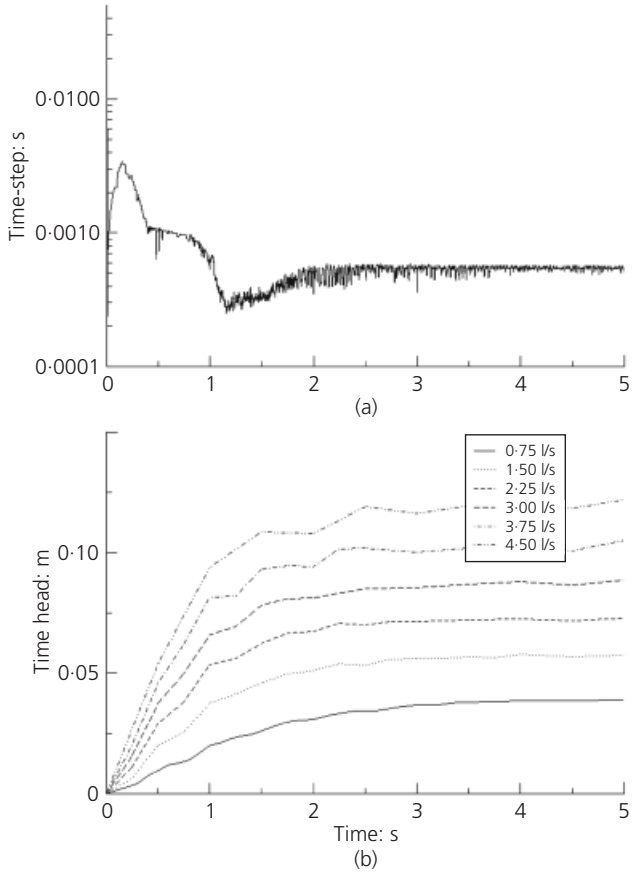

Figure 3. Graphs of variable time-step (a) and convergence (b) of the simulations

4. Results

Calculations were run in parallel on four cores of an Intel Core I7 CPU950 3·07 GHz. Typical execution times were around 44 h for each calculation.

The depth of water above the crest can be determined using OpenFOAM's sample utility along a vertical line at the outlet. The air/water interface was defined at a value of phase fraction $\alpha = 0{\cdot}5$. The exact value taken for the free surface can have a large impact on the final results. The continuity equation $Q = vA$ was solved at the outlet to calculate the average velocity of the flow. In order to estimate the wetted area A, the free surface was assumed to be horizontal. For the circular outlet, A can be expressed in terms of the hydraulic head h (water depth above the crest) and the diameter D of the outlet

$$A_{circle} = \frac{D^2}{4}\cos^{-1}\left(\frac{D-2h}{D}\right) - \left(\frac{D}{2}-h\right)(Dh-h^2)^{1/2} \quad (10)$$

Similar equations can be derived for the triangular and square outlet shapes

$$A_{triangle} = h^2 \tan\frac{\theta}{2} \quad (11)$$

$$A_{square} = b \times h \quad (12)$$

where $\theta = \pi/3$ describes the bottom angle of the triangular outlet and b is the base of the square outlet. Figure 4(a) shows a head–discharge graph, comparing the results generated by computational simulations and experimental data reported by Worrall (2011). The three different outlet shapes (circular, triangular and square) were investigated at flow rates ranging from 0·5 to 4·5 l/s. The percentage error between CFD and the experimental data can be plotted to understand Figure 4 further.

It is conventional to link the actual discharge Q and the ideal discharge Q_{ideal} through an experimentally derived discharge coefficient C_d as $Q = C_d Q_{ideal}$. This discharge coefficient accounts for contraction effects in the *vena contracta* due to a non-uniform velocity distribution in the VFC and a non-atmospheric

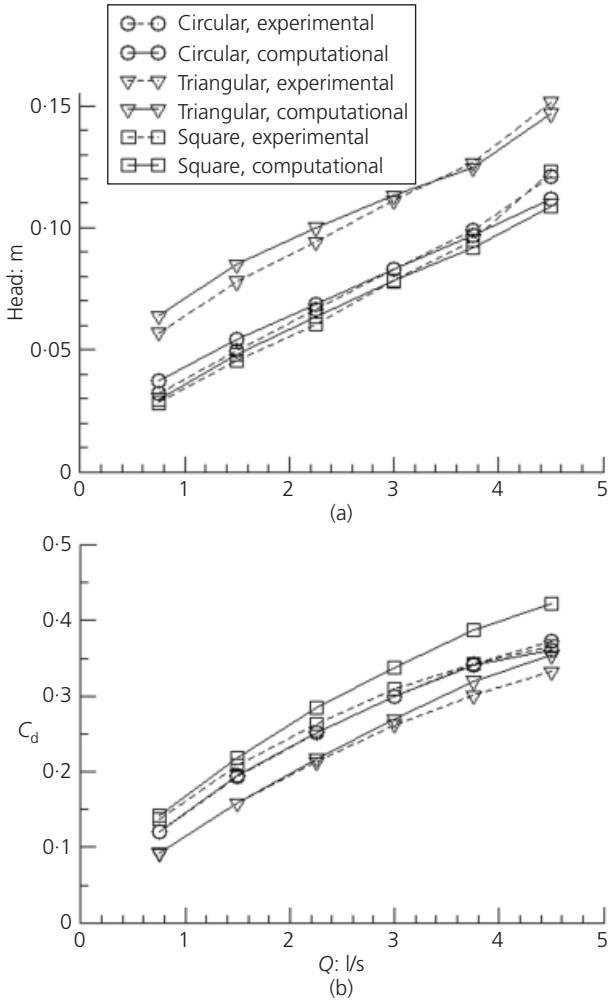

Figure 4. (a) Total head against discharge for various outlet geometries. (b) Discharge coefficient plotted against discharge

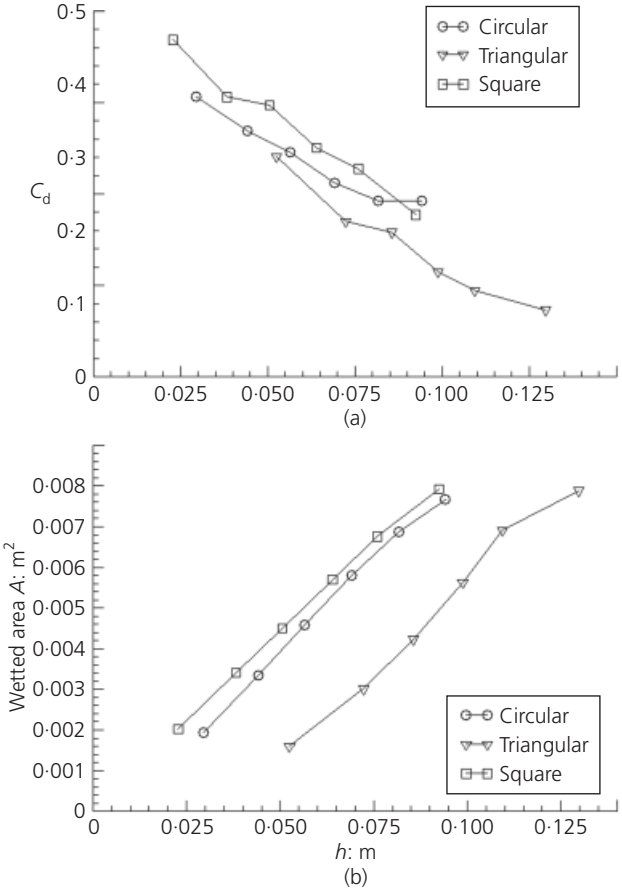

Figure 5. Comparison of computational discharge coefficient (a) and wetted area (b) against hydraulic head

pressure distribution over the crest. The discharge coefficients evaluated by means of the results of the computational simulations were calculated by rearranging Torricelli's theorem

$$C_d = \frac{Q}{A(2gh)^{1/2}} \quad 13.$$

where A was calculated using Equations 10–12. The results of a comparison study between experimental and computational discharge coefficients for various outlet geometries are shown in Figure 4(b). The experimental data were extracted from the work of Worrall (2011). In addition, Figure 5(a) presents the computational values of discharge coefficient C_d against hydraulic head h and Figure 5(b) shows the wetted area A plotted against h for various outlet geometries.

Figure 6 depicts the evolution of the flow through the domain for the circular outlet with an incoming volumetric flow rate of $Q = 3$ l/s. The results are visualised using contours of phase fraction on a vertical 2D slice through the axis of the VFC. The background indicates the position of the free surface. The air phase is defined by $\alpha = 0$ and the water phase is described by $\alpha = 1$. As before, the free surface is simulated using a contour with a fixed value of $\alpha = 0{\cdot}5$.

Figure 7 shows a comparison of computational and experimental discharge coefficients for circular, triangular and square outlets against the filling ratio (the ratio of hydraulic head to weir height, h/L). Figure 7 also shows values taken from empirical formulae for thin plate weirs derived for circular sharp-crested weirs (Vatankhar, 2010), V-notch weirs (Lenz, 1943) and rectangular sharp-crested weirs (Bagheri and Heidarpour, 2010; Emiroglu *et al.*, 2011). The computational results agree very closely with the experimental results, while agreement with the generic empirical formulae is only approximate, as might be expected.

5. Discussion

CFD was carried out in comparison with a physical model operated at various flow rates to characterise the total head–discharge curve for circular, triangular and square outlets, as

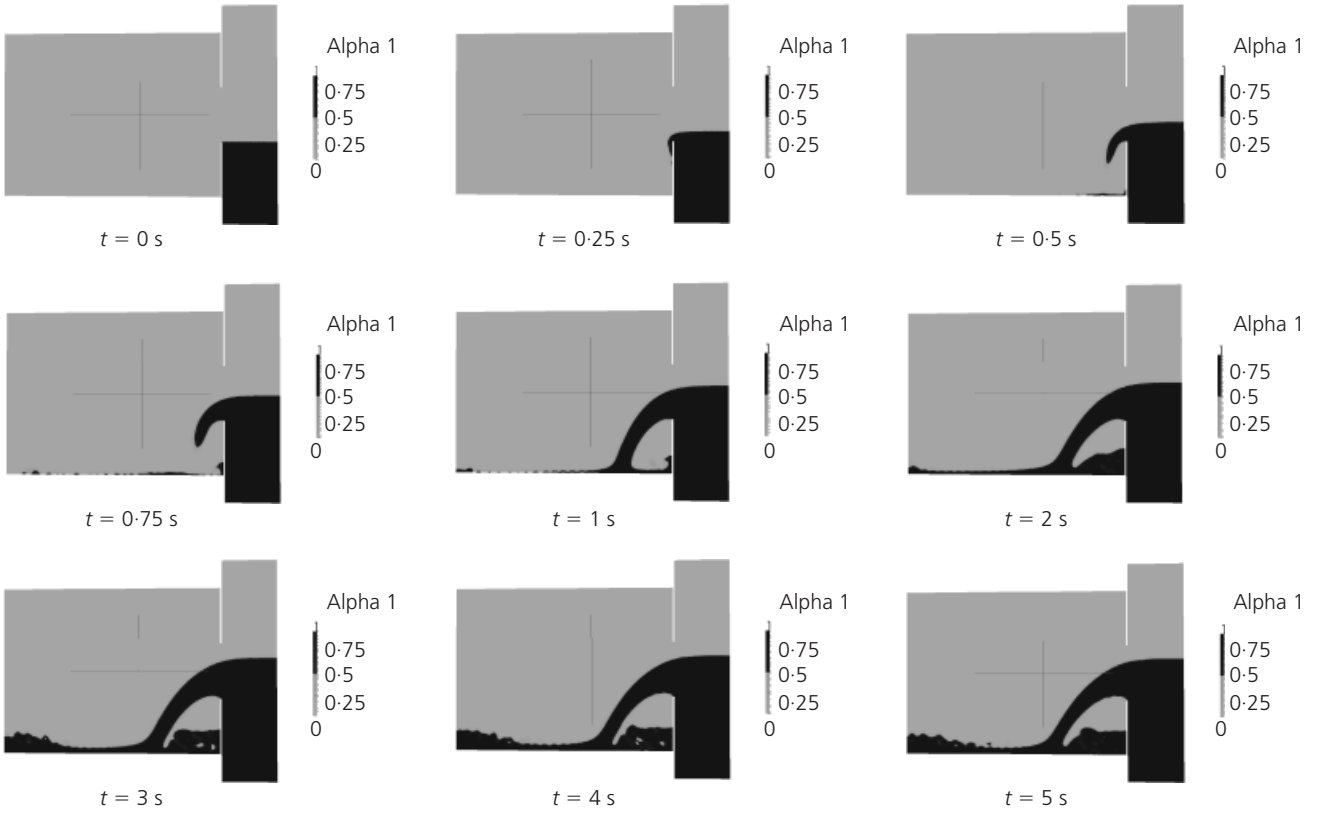

Figure 6. Visualisation of the flow evolution through the VFC at different times, t, for a flow rate of $Q = 3$ l/s, using a 2D slice through the middle of the domain

shown in Figure 4(a). For the three geometries, the prediction of total head values agreed very well with the experimental results. For $Q \leqslant 2{\cdot}7$ l/s, the computed results were slightly overpredicted, with a maximum percentage error of 16% occurring at 0·75 l/s for the circular outlet. Relative to the experimental data, this 16% difference barely exceeded the experimental uncertainty of ± 5 mm (equivalent to 14% error for this flow rate). For much of the range $3{\cdot}6 \leqslant Q \leqslant 4{\cdot}5$ l/s, the total head was underpredicted. It was observed that the sudden increase in total head occurring at the onset of the flush flow, at which the vortex initiated at around 4·5 l/s, was underpredicted for the triangular and square outlets. However, the flow here is unstable and moving into the vortexing flow regime, and under these conditions the modelling attempted here is likely to be less accurate. As seen in Figure 4(a), the CFD was able to produce accurate results over most of the range $0 \leqslant Q \leqslant 3{\cdot}75$ l/s before the flow initiated vortices. This demonstrated the accuracy to which CFD was able to reproduce the head–discharge relationship at low flow rates.

The CFD also generated significantly higher values of total head for the triangular outlet, which was in perfect agreement with the experimental data. The circular and square outlets exhibited similar results, although the circular outlet demonstrated slightly higher head values than the square outlet. This difference in total head values for various outlet shapes can be related to the discharge coefficient C_d by rearranging Torricelli's theorem to solve for h so that

$$h = \frac{Q^2}{2gC_d^2A^2} \tag{14}$$

Substituting Equation 14 into Bernoulli's equation, the total head equation can be expressed as

$$H = \frac{Q^2}{2gA^2}\left(1 + \frac{1}{C_d^2}\right) \tag{15}$$

Thus, the total head is a function of the discharge Q, wetted area A and discharge coefficient C_d. From Equation 15, the total head can be expressed in terms of the inverse of the square of the discharge coefficient C_d. Figures 4 and 5(a) show that the discharge coefficient of the triangular outlet was always signifi-

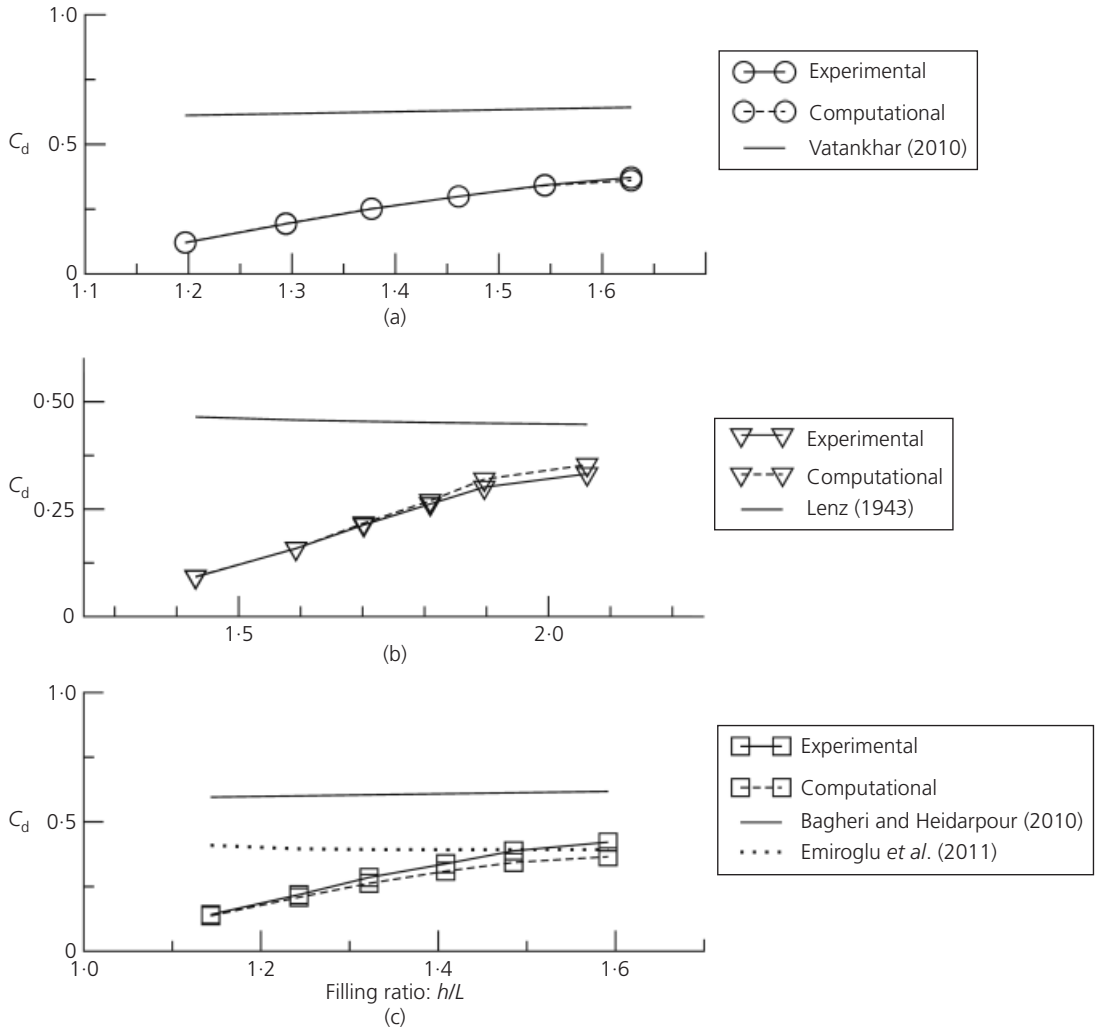

Figure 7. Comparison of discharge coefficients using computational, experimental and theoretical methods for circular (a), triangular (b) and square (c) outlets

cantly smaller than that of the circular or square outlet at a given flow rate Q and hydraulic head h.

After examination of head loss graphs across the VFC, it appeared that the geometry of the outlet had a minimum impact on the head loss. Therefore, the value of hydraulic head stayed approximately unchanged for the three geometries at a given flow rate. Moreover, the bottom of each geometry was located at a slightly different height. This was because the centre of gravity was taken into consideration to coincide with the centre of the VFC. In order to compare accurately the effect of various geometries on the values of total head, the three outlet shapes had to be compared for given values of hydraulic head h. Figure 5 shows the discharge coefficient and wetted area against hydraulic head. It was noticed that the discharge coefficient decreased, due to Equation 13. As expected, the wetted surface area at the outlet of the VFC increased as the level of water rose. The triangular outlet exhibited a smaller wetted area compared with that of the circular geometry for a given value of h. For the same value of hydraulic head h, the square outlet gave the largest wetted area. The wetted area defined the velocity of the outflow and therefore constituted an important parameter influencing the total head H.

Despite very good agreement between the computational and experimental results, some discrepancies were observed in Figure 4. These discrepancies can be explained by some of the assumptions made to simplify the computational modelling of the VFC. The experimental facilities used to investigate the VFC included a VFC in a large tank. In order to simplify the inlet boundary conditions and to save computational time, the VFC was, however, modelled without the tank. The evolution of the interface separating the two different phases was described using the phase fraction α, which cannot describe a sharp free surface. A value of $\alpha = 0{\cdot}5$ was therefore chosen to characterise the air/water inter-

face. This definition of the free surface was essential since it determined hydraulic head value to an accuracy of approximately $\pm 7{\cdot}5$ mm. In addition, the free surface was assumed to be horizontal to calculate the wetted area and therefore evaluate the velocity of the outflow.

Figure 4(b) shows computational and experimental discharge coefficients plotted against discharge while Figure 7 compares computational, experimental and theoretical discharge coefficients against filling ratio h/L. The theoretical equations proposed by Vatankhar (2010), Lenz (1943) and Bagheri and Heidarpour (2010) were derived for sharp-crested weirs perpendicular to the flow direction and located in straight, rectangular, main open channels. The discharge coefficient was found to be highly dependent on the approach conditions of the flow (i.e. hydraulic head to depth below crest ratio h/P and weir width to channel width ratio b/B). Emiroglu *et al.* (2011) proposed an equation for the discharge coefficient of rectangular side weirs in sub-critical flow conditions. The values of discharge coefficient calculated using the equation proposed by Emiroglu *et al.* agreed very well with the computed values, in particular at filling ratios approaching $h/L = 1{\cdot}6$ (Figure 7(c)). It was thus concluded that the VFC with a square outlet exhibited a similar behaviour to a rectangular sharp-crested side weir and that the equation proposed by Emiroglu *et al.* is adequate to determine discharge coefficients for filling ratios approaching $h/L = 1$. The discrepancies occurring at low values of filling ratios were attributed to the low values of Froude numbers uncovered by the equation, and also by the average percentage error of 4·54% introduced by the equation. Due to the limited amount of research published on side weirs, no similar side weir equations were found for the circular and triangular outlets.

Figure 6 shows a vertical section through the middle of the domain, where the overspilling water passed through the circular outlet for an initial incoming flow rate of $Q = 3$ l/s. The flow was visualised at $t = 0$, 0·25, 0·5, 0·75, 1, 2, 3, 4 and 5 s. At $t = 0$ s, the level of water was set below the outlet by initialising the internal field appropriately. At $t = 0{\cdot}25$ s, the nappe clung to the downstream face of the outlet. Such conditions arose for low values of discharge, where the effects of viscosity and surface tension combined to result in unstable and fluctuating flow conditions (Chadwick *et al.*, 2004). Since the values of hydraulic head were very small at low flow rates, accurate estimation of the discharge coefficient became difficult. The overspilling water jet sprang clear of the outlet of the VFC for $t \geqslant 0{\cdot}5$ s. As the jet impacted the downstream pipe, water flowed out of the domain due to a greater water depth between the VFC and the falling jet compared with the water depth downstream of the point of impact. As seen in Figure 3(b), the hydraulic head converged at approximately $t = 2$ s. For low flow rates, the hydraulic head converges to a steady value; although there is some evidence of a small fluctuation for the higher flow rates, this is thought to be minor in the context of the current analysis – it may be related to the onset of transition to the vortexing regime.

6. Conclusions

This paper has reported on the computational modelling and investigation of a VFC operated at flow rates in the range $0 < Q \leqslant 4{\cdot}5$ l/s to characterise total head–discharge curves for circular, triangular and square outlets. Multi-phase flow modelling and the VOF method were used to capture the flow pattern at the outlet of the VFC. The evolution of the interface separating the two phases was described using a discrete function, whose value in each cell of the computational domain was equal to the phase fraction so that $\alpha = 1$ for water and $\alpha = 0$ for air. The turbulent evolution of the two-phase flow was reproduced by solving the RANS equations with the k–ε turbulence model.

Validation of the computational results was carried out by analysing the total head and discharge coefficient for the three outlet shapes at various flow rates and comparing them with experimental data (Worrall, 2011). The very good agreement between the CFD and experimental results demonstrates the accuracy to which the combination of the VOF method and the k–ε turbulence model is able to reproduce the head–discharge relationship. The triangular outlet exhibited significantly higher values of total head due to a smaller discharge coefficient and smaller wetted area for a given value of hydraulic head. The total head was found to be a function of the discharge Q, discharge coefficient C_d and wetted area A.

The computational and experimental discharge coefficients were also compared with theoretical results. The proposed equations for sharp-crested weirs in open, rectangular channels failed to predict the C_d values due to the swirling pattern of the flow introduced by the tangential inlet of the VFC. The values of C_d calculated using the equation for rectangular sharp-crested side weirs proposed by Emiroglu *et al.* (2011) agreed well with the computed values, in particular at filling ratios approaching $h/L = 1{\cdot}6$. The discharge coefficient was found to be highly dependent on the approach conditions of the flow.

REFERENCES

Bagheri S and Heidarpour M (2010) Flow over rectangular sharp-crested weirs. *Irrigation Science* **28(2)**: 173–179.

Berberovic E, Van Hinsberg NP, Jarkirlic S, Roisman IV and Tropea C (2009) Drop impact onto a liquid layer of finite thickness: dynamics of the cavity evolution. *Physical Review E* **79(3)**: 036306.

Chadwick A, Morfett J and Borthwick M (2004) *Hydraulics in Civil and Environmental Engineering*, 4th edn. Spon, London, UK.

Deamer A (1988) *The Fluid Mechanics of Hydraulic Brakes for Flood Control*. MSc thesis, University of Oxford, Oxford, UK.

Emiroglu ME, Agaccioglu H and Kaya N (2011) Discharging capacity of rectangular side weirs in straight open channels. *Flow Measurement and Instrumentation* **22(4)**: 319–330.

Ferrari A (2010) SPH simulation of free surface flow over a sharp-crested weir. *Advances in Water Resources* **33(3)**: 270–276.

Gopala V and Wachen BV (2007) Volume of fluid methods for immiscible-fluid and free surface flows. *Chemical Engineering Journal* **141(1–3)**: 204–221.

Green M (1988) Flow control evaluations. *Proceedings of Conflo 88 – Attenuation Storage and Flow Control for Urban Catchments*. Oxford University Press, Oxford, UK.

Hirt C and Nichols B (1981) Volume of fluid method for the dynamics of free boundaries. *Journal of Computational Physics* **39(1)**: 201–225.

Issa RI (1985) Solution of the implicitly discretised fluid flow equations by operator-splitting. *Journal of Computational Physics* **62(1)**: 40–65.

Jarman D (2011) *A Study of the Design of Cylindrical Vortex Flow Controls for use in Urban Drainage Systems*. PhD thesis, University of Exeter, Exeter, UK.

Jasak H and Weller HG (1995) *Interface Tracking Capabilities of the Inter-gamma Differencing Scheme*. Imperial College of Science, Technology and Medicine, London, UK.

Kulkarni A, Ranade V, Rajeev R and Koganti S (2008) Pressure drop across vortex diodes: experiments and design guidelines. *Chemical Engineering Science* **64(6)**: 1285–1292.

Launder BE and Spalding DB (1974) The numerical computation of turbulent flows. *Computer Methods in Applied Mechanics and Engineering* **3(2)**: 269–289.

LeCornu JP and Faram MG (2006) Evolving methods for the calibration of flow controls for stormwater and wastewater management. *Proceedings of CIWEM 4th Annual Conference, Newcastle, UK*. Chartered Institution of Water and Environmental Management, London, UK.

Lenz A (1943) Viscosity and surface tension effects in v-notch weir coefficients. *Transactions of ASCE* **108(1)**: 758.

Leonard B (1988) Simple high-accuracy resolution program for convective modeling of discontinuities. *International Journal for Numerical Methods in Fluids* **8(10)**: 1291–1534.

Parsian H and Butler D (1993) Laboratory investigation into the performance of an in-sewer vortex flow regulator. *Water and Environment Journal* **7(2)**: 182–189.

Priestman G (1987) A study of vortex throttles. Part 1: experimental. *Proceedings of the Institute of Mechanical Engineers Part C* **201(5)**: 331–336.

Qu J, Ramamurthy AS, Tadayon R and Chen Z (2009) Numerical simulation of sharp-crested weir flows. *Canadian Journal of Civil Engineering* **36(9)**: 1530–1534.

Sarker M and Rhodes D (2004) Calculation of free-surface profile over a rectangular broad-crested weir. *Flow Measurements and Instrumentation* **15(4)**: 215–219.

Tabor GR (2010) OpenFOAM(tm): an Exeter perspective. In *ECCOMAS CFD 2010, Lisbon, Portugal* (Pereira JCF and Sequeira A (eds)), CD-ROM.

Vatankhar A (2010) Flow measurement using circular sharp crested weirs. *Flow Measurement and Instrumentation* **21(2)**: 118–122.

Weller HG, Tabor G, Jasak H and Fureby C (1998) A tensorial approach to computational continuum mechanics using object orientated techniques. *Computers in Physics* **12(6)**: 620–631.

Wojtowicz P and Kotowski A (2009) Influence of design parameters on throttling efficiency of cylindrical and conical vortex valves. *Journal of Hydraulic Research* **47(5)**: 559–565.

Worrall E (2011) *Experimental Testing and Analysis of Modified Vortex Flow Control at Hydro International plc*. University of Exeter, Exeter, UK, Report I2.